Saturn's Ring-Plane Crossings of August and November 1995: A Model for the New F-Ring Objects

François Poulet[1]

Observatoire de Paris, 92195 Meudon Cédex Principal, France
E-mail: francois.poulet@obspm.fr

Bruno Sicardy

Observatoire de Paris/Institut Universitaire de France, 92195 Meudon Cédex Principal, France

Philip D. Nicholson

Center for Radiophysics and Space Research, Cornell University, Ithaca, New York 14853-6801

Erich Karkoschka

Lunar and Planetary Laboratory, University of Arizona, Tucson, Arizona 85721

and

John Caldwell

Department of Physics and Astronomy, York University, 4700 Keele Street, North York, Ontario, Canada M3J 1P3

We analyze observations made in August and November 1995 during the Earth and Sun crossings of Saturn's ring plane, respectively. The August 1995 observations combine data taken with the Adonis adaptive optics system at the European Southern Observatory (ESO) and images from the Hubble Space Telescope (HST). The November 1995 data are based on HST images only. We report here the detections of four new objects (three in August, one in November) orbiting near, or within, the F ring of Saturn. Two of the objects observed at ESO in August 1995 are most probably S/1995 S5 and S/1995 S6, reported by P. D. Nicholson *et al.* (1996, *Science* 272, 509–515) from the HST observations on August 10, 1995. The third object, S/1995 S20 cannot be clearly linked with any other objects reported by other observers. An elongated object, or arc, is tracked in November 1995, and can be connected to one of the arcs also reported by Nicholson *et al.* Our combined measurements improve the determination of the orbital parameters of S/1995 S5 and the arc, indicating that these objects orbit, within the error bars ($\lesssim \pm 140$ km), in the F ring. We discuss the nature and origin of these F-ring features. We propose that they are clouds of regolith ejecta resulting from collisions between large particles, or "parent bodies," within the F ring. From the available constraints (brightness and lifetime of the objects), we show that the observa-tions are consistent with the presence of several hundred 1-km-sized (and/or several thousand 100-m-sized) unseen parent bodies embed-ded in the F ring, each of which is covered by a regolith layer tens of centimeters to ~1 m in thickness. © 2000 Academic Press

Key Words: planetary rings, Saturn; observation; dynamics.

1. INTRODUCTION

Every 15 years or so, Earth and the Sun cross Saturn's ring plane. The scattered light from the bright main rings is then sufficiently reduced to permit the study of faint objects (rings and satellites) and to reveal new ones during a few-month pe-riod. In this context, the 1995/1996 edge-on orientation of the rings provided a special opportunity to study the Saturn sys-tem. First, it could benefit from recent advances in observa-tional techniques (infrared arrays, adaptive optics cameras, and the space telescope, all unavailable during the previous cam-paign of 1979/1980), and second it was the last crossing before the *in situ* observations of the Cassini orbiter, planned to start in 2004.

The observations discussed in this paper led, among other results, to the detections of new objects orbiting just outside the A ring (and more precisely, close to or within the F ring, as

discussed herein), labeled S/1995 S1, S/1995 S2, etc.[1] (Bosh and Rivkin 1996, Nicholson *et al.* 1995, 1996, Sicardy *et al.* 1996a,b, Poulet *et al.* 1997, Roddier *et al.* 1996a,b). The detection of such objects is not new, however; the Voyager images revealed in 1980/81 several condensations within the F ring (Smith *et al.* 1982). The present observations, spanning time intervals of a few days to a few months, can yield important complementary constraints as to the nature of these transient bodies.

We divide our work in two parts. In the first part (Sections 2 and 3), we concentrate on the detections of new objects near the orbit of the F ring. We use data obtained in August 1995 at the European Southern Observatory (ESO) with an adaptive optics system and also analyze data gathered by the Hubble Space Telescope (HST) in November 1995. We then combine previous HST results obtained by Nicholson *et al.* (1996), hereafter referred to as N96, with our new results to constrain the orbit and photometry of three new objects detected in August 1995 and of one ring arc feature observed in November 1995, all near or within the F ring.

In the second part of the paper (Section 4), we discuss the nature of these condensations. The F-ring region, roughly corresponding to the Roche zone of the planet, is of prime interest because of the balanced competition between satellite accretion and tidal disruption. In particular, the interplay of isolated compact bodies and continuous fluid rings probably tells us something about satellite formation processes.

According to the simulations of Salo (1992) and Hänninen (1993), the existence of the F ring is hard to understand without the existence of a significant source of dust. Because of the short lifetime of the dusty component, we need an active mechanism to create transient objects. We propose here that they are clouds of regolith ejecta resulting from collisions between larger particles (or "parent bodies") embedded within the F ring. From our observational constraints, we derive the lifetime of these objects, the total cross-sectional area and the sizes of the parent bodies, and the properties of the regolith covering their surface.

The implications of our results for the evolution of the F ring are discussed in Section 5, which also offers some concluding remarks.

2. OBSERVATIONS AND DATA REDUCTION

The Earth crossed Saturn's ring plane on May 22, 1995, around 5^h UT, and again on August 10, 1995, around 21^h UT. A third Earth crossing took place on February 11, 1996, but Saturn was then too close to the Sun on the sky to be easily observed. The Sun crossed the ring plane during the interval November 17–21, 1995. The data analyzed here involve the August and November 1995 ring plane crossings ("RPXs" for short), as described below.

2.1. August 1995 ESO Observations

These groundbased observations were carried out during a six-night period bracketing the August 10 crossing. We used the ADONIS (former COME-ON+) adaptive optics system, mounted on the ESO 3.6-m telescope at La Silla, Chile. Poor atmospheric conditions (seeing of 1.5 arcsec) prevented the achievement of diffraction limited performance (0.1 arcsec). Nevertheless, the adaptive optics system did obtain images with mean angular resolution as low as 0.4 arcsec, with some images reaching a resolution of 0.3 arcsec. The corrected images were acquired by the 256×256-pixel SHARP II infrared camera with a scale of 0.0505 arcsec per pixel (~320 km at Saturn). Note that the field of view (12.9×12.9 arcsec) is not wide enough to contain both ring ansae (~43 arcsec tip to tip). Blocks containing 10 successive images were recorded, each image having an exposure time of either 30 or 60 s. We used a near-infrared K' filter (2.15 μm, $\Delta\lambda = 0.32$ μm), which falls within an sorption band in Saturn's atmosphere due to hydrogen and methane, in order to reduce the contribution of scattered light from the planet disk.

Only the nights of August 9 and 10, when the dark (southern) side of the rings was visible, were used to search for small inner objects. During this period, the elevation of Earth with respect to the ring plane changed from $-0.045°$ to $-0.013°$, while the rings were illuminated by the Sun at an elevation angle of $+1.5°$. The faintness of the A and B rings makes the detection of faint objects relatively easy in these regions.

2.2. November 1995 HST Observations

Images were obtained by the HST during three orbits on November 17 and 18, 1995. The data of November 17 come from an observing program by Tomasko and Karkoschka (program ID 6030), with a total of 11 suitable PC images, and a pixel size of 302 km at Saturn. The data of November 18 are from a program by Caldwell (ID 6328), with 10 wide field (WF) images. Between these two dates, the Sun started to cross the ring plane from the north to the south side, while the Earth was $2.67°$ north of the ring plane. The HST observations of N96 were all obtained on November 21, at the end of the solar crossing.

2.3. Image Processing

Standard infrared data reduction procedures were applied to each individual ESO frame: flat-fielding to correct pixel-to-pixel sensitivity variations, sky subtraction, and cosmic ray elimination. The removal of a periodic electronic pattern in the detector was also performed through a Fourier transform.

The HST data used in this analysis were the calibrated data frames provided by the Space Telescope Science Institute. Conventional flat-fielding and dark subtraction were performed during HST pipeline processing (Biretta *et al.* 1996). As the extremities of the rings are near the edge of the camera field of view, we took into account optical distortion in the HST planetary camera (Holtzman *et al.* 1995).

---

[1] For the sake of brevity, these objects will be referred to as S1, S2, etc., in this paper.

The difficulties inherent in the detection of small objects stem from the scattered light background from the planet and the rings. Furthermore, the strong local gradient of light due to the planet can systematically bias measurements of object positions. We experimented with several methods of subtracting the scattered light from the planet. For all final results (ESO and HST images), the background was determined from a robust, low-order, polynomial fit to each line parallel to the ring plane.

When there was no strong variation in the seeing, the PSF was deconvolved from the adaptive optics images. Direct linear deconvolution did not yield satisfactory results. We used instead an iterative procedure based upon the maximum likelihood algorithm. This procedure is the preferred method for identifying moving features, but it was not used for photometry purposes since the flux is not conserved. Also, the long exposure times necessary for the detection of faint objects greatly increase the residual light from the rings. Ring subtraction was performed using either an earlier or a later reference image in which no satellite appears in order to subtract the ring light in the images of interest. We first superimposed the rings in the two images, and then compared and adjusted the ring brightnesses before subtraction.

The varying exposure time and filter for the HST images and the long intervals of time between the images prevent the construction of such a template profile. In this case, we simply tracked those variations of brightness whose motion appeared to be consistent with F-ring objects.

3. RESULTS

3.1. Detections of Faint Objects

Recoveries. During the HST orbits bracketing the Earth crossing of August 10, three objects whose orbital motion could be clearly tracked were detected and designated S5, S6, and S7 (Nicholson *et al.* 1995, N96, Sicardy *et al.* 1996b). Because the time span of these observations was less than 10 h, only a fraction of their orbital periods (~14.8 h) was sampled. However, unresolved objects were also detected at ESO on the two previous nights at positions consistent with the orbits of S5 and S6 as derived by N96 (Sicardy *et al.* 1995, 1996a, Poulet *et al.* 1997). Figure 1 displays the orbital motion of S5 along the western ansa of the rings on August 9, after ring subtraction.

In the meantime, Roddier *et al.* (1996a, 1996b), also using an adaptive optics system, reported the detection of 10 objects near the F ring. Among these, S8, S9, S11, S12, S13, and S14 lay outside all of our ESO images. S15, S16, S17, and S19 were not seen in our adaptive optics data, because of interference from bright features (satellites or the Cassini division) and/or seeing limitations.

The November solar crossing added a second dimension to the images of the F-ring region, allowing us to distinguish more easily between point-like objects and ring arcs. Two arcs embedded in the F ring were detected by HST on November 21 (N96).

TABLE I
Planetocentric Measurements

Satellite	Decimal day 1995 (UTC)	Planetocentric positions[a] (km)
S5	9.24479 August	−100,853
S5	9.24549 August	−101,936
S5	9.24618 August	−102,573
S5	9.24687 August	−102,828
S20	10.34624 August	−103,000
S20	10.34693 August	−104,000
S20	10.34902 August	−105,500
S20	10.34971 August	−107,500
S20	10.35110 August	−108,500
S20	10.36956 August	−127,200
Arc10	17.34995 November	138,400
Arc10	17.35250 November	137,800
Arc10	17.35448 November	136,966
Arc10	17.35652 November	135,890
Arc10	17.35939 November	135,490
Arc10	17.36142 November	133,791
Arc10	18.35632 November	−88,007

[a] The minus sign means west ansa. See text for the uncertainties in the measurements.

We extended this search to the HST images of November 17 and 18. This was done in a less favorable photometric context, however, because the main rings were still quite bright due to direct illumination by the Sun. The shorter exposure times used for these images, on the other hand, were better adapted to detect moving objects. In particular, it is easier to distinguish between the smearing due to orbital motion and the actual azimuthal extension of the object.

These points are illustrated by Fig. 2, which shows examples of the arc detections of November 17 near the eastern ansa of the rings. This arc was spotted seven times on November 17 and 18 (Table I). We show below that its positions are consistent with that of the 10° arc (called Arc10 hereafter) described by N96. The arc has a full length at half maximum brightness of about 7.5°. This difference could be due to a shorter exposure time on November 17 (80 s instead of 300 s) and to the illumination geometry. Evolution of the structure over 4 days is also possible.

New detection. The deconvolution of a series of ESO images on August 10 produced evidence for a new object, S20, also moving at a speed consistent with the mean motion of the F ring (see Fig. 3).

3.2. Astrometry

When available, a known satellite was used as an astrometric reference point in each image. Ephemerides of the satellites were taken from the on line software at the Planetary Data System's Rings Node (Showalter 1995), which uses ephemeris files provided by the Jet Propulsion Laboratory. For the HST images in which no known satellite is available, Saturn's limb was used as a pointing reference. The edge-on ring was used to define
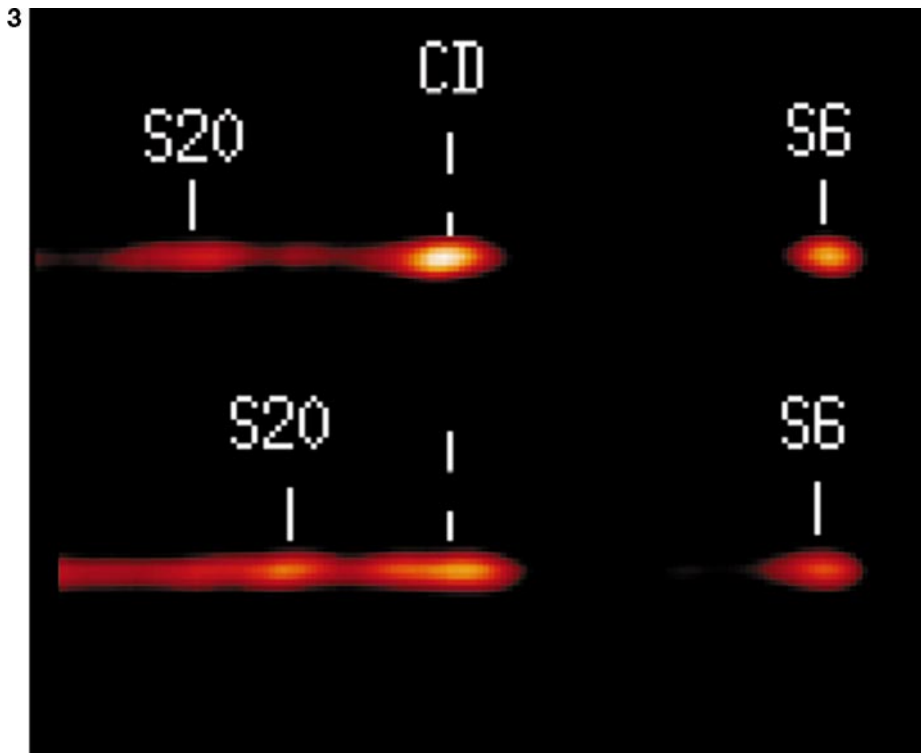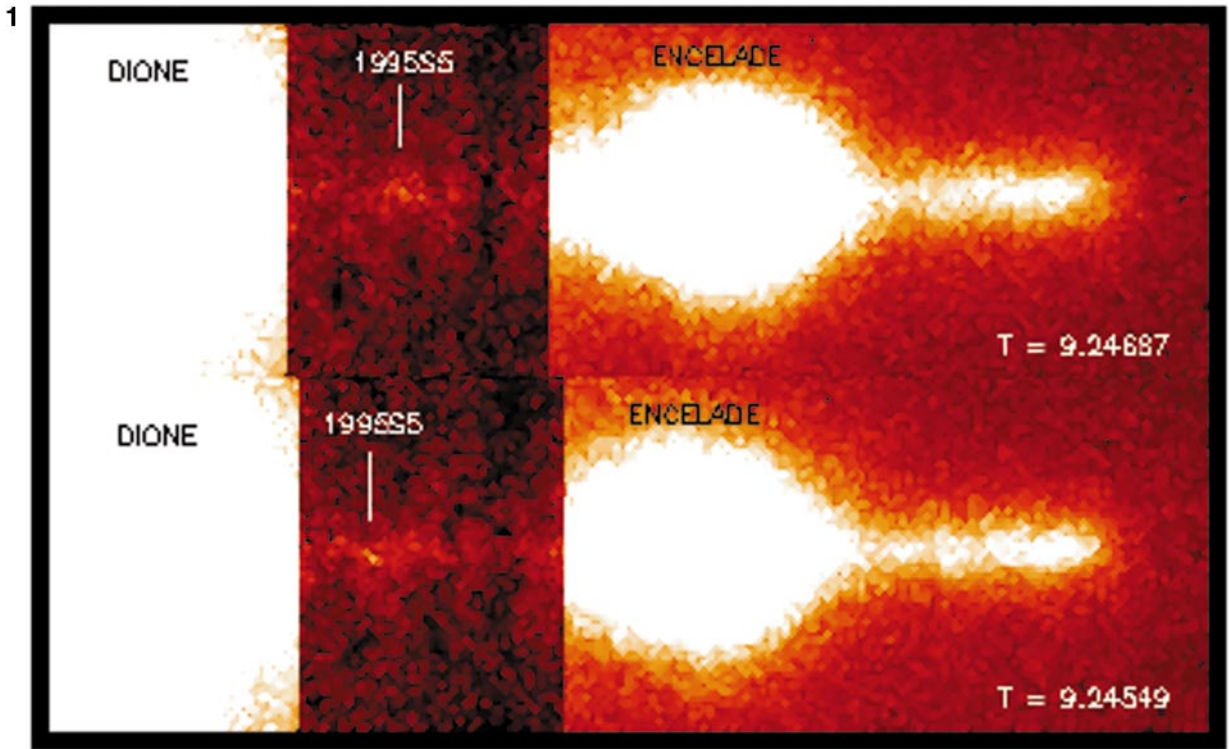
FIG. 1. The west ansa of Saturn's rings observed with the Adonis adaptive optics camera at the ESO 3.6-m telescope. Each image was taken in the K' band with a 60-s exposure and has a size of 20×12 arcsec on the sky. The time is the decimal date in August 1995 (UT), so that we see here the unlit side of the rings $\sim$39 h before Earth's ring plane crossing. A template image has been subtracted in a part of each frame to show the orbital motion of S5.

FIG. 3. Same as in Fig. 1, but on August 10, 1995, at $8^h.3097$ (top) and $8^h.4264$ (UT) (i.e., $\sim$12 h before the Earth RPX). Each image has a size of 8×3 arcsec. The images have been deconvolved by the point spread function (see text) and reveal the motion of a faint object, S20. Note the conspicuous presence of a point-like object at the tip of the rings. This sharp increase of signal (which is not observed in other ESO images) probably corresponds to S6, observed a few hours later by the Hubble Space Telescope (see N96 and the text). CD indicates the brightening due to the Cassini Division. The A ring is not visible in these images because of the choice of stretch.
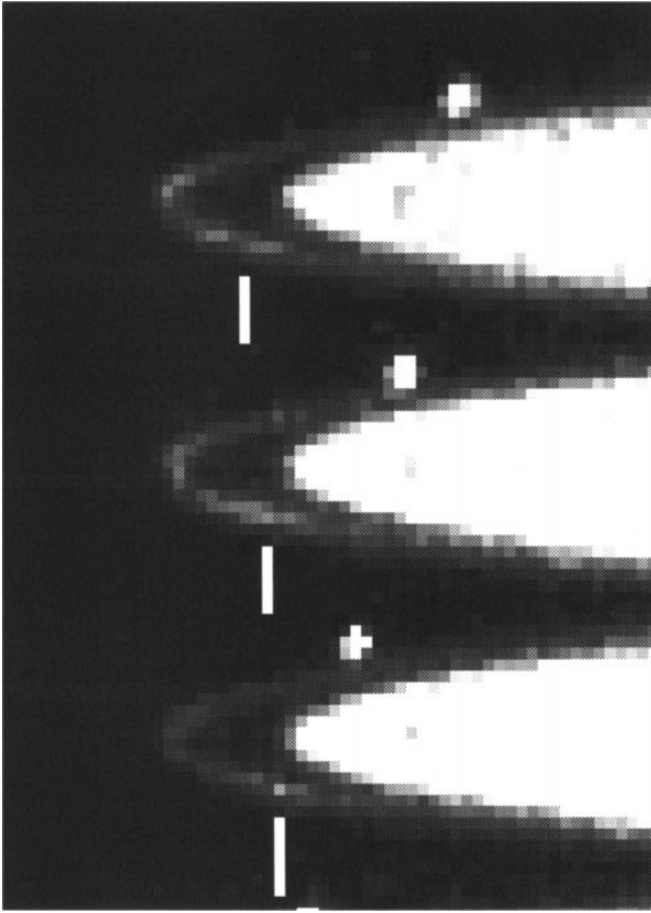
138

FIG. 2. Sequence of three magnified HST images taken on November 17, 1995, showing the eastern ansa of the A ring and the detached F ring. Each image has a size of 10.75×4.6 arcsec. They were taken at mid-times of 08:23:56 (top), 08:27:36 (middle), and 08:30:24 UT (bottom), with integration times of 80 s, 40 s, and 18 s in the $\lambda = 0.34$ μm, $\lambda = 0.41$ μm, and $\lambda = 0.47$ μm filters, respectively. The solar RPX started a few hours later, so that we see the lit side of the rings under grazing illumination with an elevation angle of $2.67°$ for the observer. The object moving in the upper part is Epimetheus, and the vertical bars indicate the motion of the object Arc10.

the north–south location of Saturn's center. The positions of the various sources were determined by a centering routine for the brighter satellites and by picking "by eye" the brightest pixel for the fainter ones. The pixel locations were then converted to distances from Saturn, as projected onto the plane of the sky.

The temporal coverage of our data set is summarized in Fig. 4, where the observed planetocentric positions vs time are plotted together with circular orbit fits. The S5 and arc detections reported here permit us to improve their orbital parameters with respect to the initial values reported by N96. This is not the case for S6, since we have groundbased observations only at greatest elongation. The planetocentric positions given in Table I combined with the positions measured by N96 constitute the final input to the various orbital solutions.

The uncertainties assigned to these measurements depend on the number of individual measurements combined in each point,

the uncertainties in these measurements, and systematic errors in the pointing reference. For the HST data, we have compared the determination of Saturn's center using a satellite and using the limb of the planet. Both methods agree to within ± 0.04 arcsec for PC images (0.9 pixel), and ± 0.07 arcsec for WF images (0.7 pixel). So, taking into account the uncertainty in the center of the objects, we assign uncertainties of ± 0.06 arcsec for the PC data, vs ± 0.12 arcsec for the WF images, i.e., about $\pm 0.16°$ and $\pm 0.31°$ in longitude for an object orbiting near the F ring.

The August 1995 dark side ring profiles extend to the location of the F ring (140,200 km), which was used as an astrometric reference in some of the ESO images. Comparisons of various ESO profiles allow us to estimate uncertainties of ± 0.1 arcsec ($\sim$2 pixels). Considering the uncertainties in the determination of the photocenter of S5, we estimate uncertainties of ± 0.20 arcsec for the ESO positions.

3.3. Orbital Solutions

The combination of groundbased and HST observations near August 10 and November 21, 1995, allows us to cover several revolutions of each object (except for S20). The observed positions are fitted to circular, noninclined orbits. Given the possibility that these objects actually lie within the F ring, we also performed a second set of noncircular orbital fits using the eccentricity e and longitude of pericenter $\tilde{\omega}$ of the F ring (N96). Note that the radius a is fitted independently of the mean motion n. Consequently, we also calculate a semimajor axis a_{calc} from n, using the mass of Saturn $GM_S = 37{,}931{,}272$ km^3 s^{-2}, a reference radius $R_S = 60{,}330$ km, and including the effects of $J_2 = 16{,}298 \times 10^{-6}$, $J_4 = -915 \times 10^{-6}$, and $J_6 = 103 \times 10^{-6}$ (Campbell and Anderson 1989).

Table II gives the derived orbital elements of S5, S20, and Arc10, namely the radius a, the mean-motion n, and the longitude λ_0 at epoch (August 10^d 12^h, 1995, TDT, at Saturn, and November $21^d 12^h$, 1995, TDT, at Saturn, respectively). Longitudes are measured from the ascending node of Saturn's equatorial plane on Earth's equatorial plane (J2000). The errors in the orbital elements are obtained by introducing random errors in the positions, within the quoted limits of uncertainties. The RMS residuals for all the points (namely $\sim$0.06 arcsec for S5 and $\sim$0.12 arcsec for Arc 10) are comparable to the errors in the position measurements.

Based on a circular orbit fit, S5 lies between the orbits of Pandora and Prometheus. Our analysis yields a semimajor axis for S5 which lies closer to the F ring radius ($140{,}220 \pm 5$ km, Bosh and Olkin 1997) than that previously derived by N96, using the HST data of August 10 only. Including the eccentricity and orientation of the F ring orbit in the fit does not improve the rms residuals and thus does not provide further information as to the association of S5 with the F ring.

We cannot fit an orbit for S20 with our positions only, which correspond to a time span of half an hour or so (Table I). However, if we assume it is an F-ring clump, then we can fix a and e and solve for λ_0.
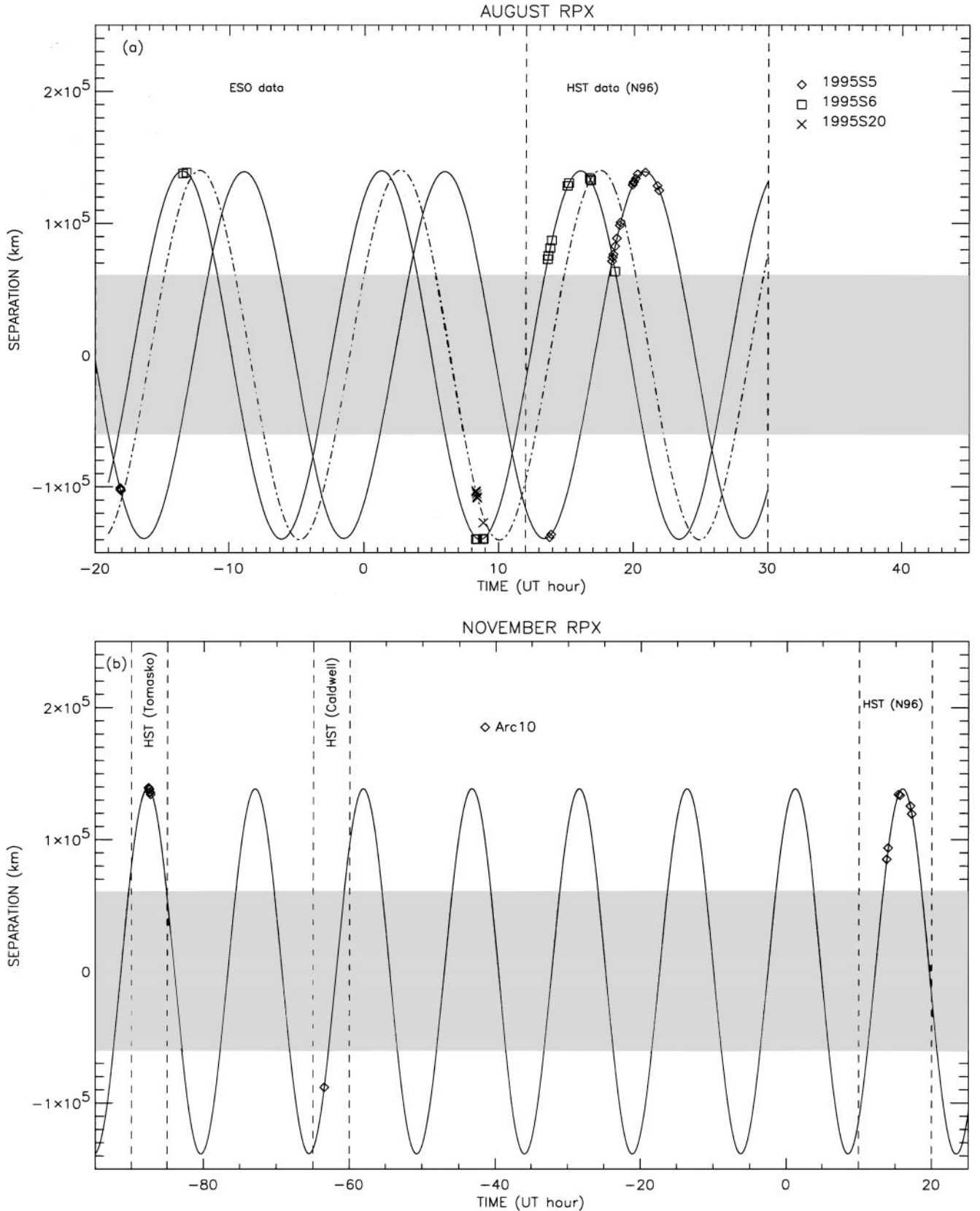
FIG. 4. (a) Measured planetocentric offsets (km) vs time (hours) for S5 (diamonds), S6 (squares), and S20 (crosses). The origin of time is August 10, 1995, 0:00 (UT). The offsets are positive eastward. The shaded band represents the planet and the dashed lines indicate the various intervals of observations. Circular orbit fits for S5 (solid line), S6 (solid line), and S20 (dot-dashed line) are superimposed. Table II gives the derived orbital elements for S5 and S20; the S6 orbital elements are given by N96. (b) A similar plot for the Arc10 detections during the solar RPX. The origin of time is November, 21, 1995, at 0:00 (UT).

TABLE II
Orbital Elements for S5, S20, and Arc10

Parameters	S5	S5	S20	Arc10	Arc10
a (km)	139775 ± 260	139936 ± 220	140200^a	138124 ± 1100	138746 ± 1050
n (degrees/day)	581.70 ± 0.40	582.06 ± 0.30	582.05^a	583.06 ± 0.22	582.90 ± 0.20
λ_0 (degrees)	130.35 ± 0.10	130.80 ± 0.10	211.0 ± 2.0	244.18 ± 0.09	243.91 ± 0.08
e	0^a	0.0029^a	0^a	0^a	0.0029^a
ω (degrees)	—	14.4^a	—	—	292.5^a
RMS (km)	430	400	1143	854	821
a_{calc} (km)	140266 ± 60	140208 ± 50	—	140048 ± 35	140074 ± 30

Note. The uncertainties are 1σ errors.
[a] Assumed.

We determine the orbital parameters of Arc10 by fitting the positions of the mid-point of the elongated arc. The global data coverage of seven revolutions substantially improves the mean motion determination, and the revised semimajor axis appears to be consistent with the F-ring location (see Table II): the calculated semimajor axis is $a_{\text{calc}} = 140{,}074 \pm 30$ km, i.e., 5σ away from that of the F ring, $a_{\text{F}} = 140{,}220 \pm 5$ km (Bosh and Olkin 1997). However, the multiple strands of the F ring spread over more than 200 km (Murray *et al.* 1997), strongly suggesting a close association of Arc10 with the F ring. Note also that the extended structure of the arc combined with the noise may induce errors in its position and thus explain in part the discrepancy between a_{calc} and a_{F}.

3.4. Photometry

Complementary information on the new objects can be gathered from photometry. From the integrated flux, and assuming a spherical shape with Pandora's albedo, we can estimate the equivalent radius for the new objects. Obviously, the derived values are meaningful only if the new objects are compact moons. The estimated equivalent radius of S5 from ESO data is about 20 km.

The photometry of S6, detected from ESO at the tip of the ring ansa, is not very accurate because of the difficulty in subtracting the light from the ring in a region of strong gradient. However, we can compare the brightness of S6 with that of Pandora, seen at the same absolute planetocentric distance. It turns out that S6 must have at least the same equivalent radius, 45 ± 5 km, as Pandora. N96 find a significantly smaller value (18 ± 5 km); the simplest explanation of this difference is that S6 is an elongated object in the direction of its orbital motion. Thus, all the flux is integrated in one pixel when S6 is observed at the ansa, while it is diluted (and thus partially lost) in the background F ring when it is observed elsewhere.

While the direct deconvolution is linear and preserves the photometry, the maximum likelihood deconvolution allows only a morphological study. This prevents the measurement of the brightness of S20, which is seen only after deconvolution. A rough estimation of its brightness gives an equivalent radius of the order of 15 km.

In any event, the derived equivalent radii for S5 and S6 lead to estimated sizes larger than those of Pan and Atlas, which have not been detected. It is unlikely that such moons were missed during the Voyager encounters. Therefore, the new objects are probably transient F-ring clumps, confirming the conclusions of N96 and Bosh and Rivkin (1996). What conclusions about their lifetimes can be derived from the present observations? New constraints have been obtained by McGhee *et al.* (1998), who carefully examined the different HST data sets. Of the satellite candidates observed in May and August 1995, only S7 has a possible match and appears to be coorbital with Prometheus. Extrapolating the other clump positions observed in August to November 1995 does not yield obvious correlations (N96, McGhee *et al.* 1998). The HST data of May 1995 (Bosh and Rivkin 1996) reveal clearly only one new object vs several in August and November. This implies lifetimes of at most a few months for these objects. Our data support these conclusions. For instance, the extrapolated position of Arc10, the most obvious F-ring candidate, from November to August does not reveal any correlation with S5, S6, or S7. The analysis of the Voyager 1 and 2 F-ring images by Showalter (1997) shows that the detected clumps propagate with mean motions in the range $582.1 \pm 0.3°$/day. Considering this interval, only S14 (Roddier *et al.* 1996b) could be linked with Arc10. However, the large difference of brightness between these two objects makes the possibility of a single, unchanging object unlikely.

4. DISCUSSION

4.1. Nature and Lifetime of the F-ring Objects

The presence of clumps in the F ring could be the result of purely kinematic processes, associated with the perturbations of Prometheus and Pandora (Showalter and Burns 1982). However, in a numerical study of the F ring, Hänninen (1993) considers the generation of clumps by the shepherd satellites, taking into account interparticle collisions. This author identifies various clumps after one synodic period of Prometheus, but they exhibit little density contrast because of azimuthal overlapping, and would remain undetected in the actual F ring.

Another explanation is that collisions between larger particles (or "parent bodies") embedded in the F ring can release regolith and form clouds of dust, thus explaining the transient objects observed in the F ring. The concept of a belt of colliding parent bodies in the neighborhood of the F ring was first advanced by Cuzzi and Burns (1988) to explain the abrupt depletions in the flux of magnetospheric electrons detected by Pioneer 11. The presence of large bodies has been investigated in other dusty rings similar to the F ring. For instance, in addition to a large dust component, Saturn's G ring may contain a population of large bodies (a few kilometers in radius) responsible for the production and maintenance of the dust component (Canup and Esposito 1997).

Actually, both the F-ring core and its dusty envelope have particle size distributions compatible with collisional and disruptive processes (Showalter et al. 1992). The PPS profile shows that the core region has a maximal normal optical depth $\tau_N \sim 0.4$, whereas the average τ_N of the 50-km-wide envelope of the system is about 0.1 (Showalter et al. 1992). Consequently, collisions between ring particles must be frequent, namely of the order of one per day per particle.

Let N_{cl} be the total number of clumps in the F ring at a given time, each with a typical mass M_{cl} and lifetime T. This requires a total mass rate of regolith injected into the F ring through collisions of

$$\dot{M}_{reg} = (N_{cl} M_{cl})/T. \qquad (1)$$

In order to estimate the value of $\dot{M}_{reg}$, we examine in turn the various quantities which enter this equation. Then, in the next subsection, we will see how collisions between parent bodies can provide such a quantity of dust per unit time in the F ring.

Mass of the clumps.   The quantity M_{cl} depends on geometrical factors, like the length, width, and height of the clump, and on its density, which is related to its optical depth. During the Earth ring plane crossing, the contribution of the F ring dominates the residual flux of the whole system. In Poulet et al. (2000), we model the F ring as a ribbon of radial width W, radial optical depth (along W) τ, and physical height H. This ribbon is supposed to contain large particles embedded in dust. We show that, on the average, the edge-on profiles yield $\tau \sim 0.2$ for the ring. If we assume that the average F ring and the clumps have the same photometric properties, a temporary brightening can occur if a swarm of particles is created. The difference in radial optical depth, $\Delta\tau$, between that clump and the average F ring will lead to a local contrast $\frac{\Delta\tau}{\tau}$ in brightness. The HST August 10, 1995, images constrain the value of $\frac{\Delta\tau}{\tau}$ for the three objects S5, S6, and S7, with typical values between 2 and 3.

Let L_{cl} and H_{cl} be the length and the height of the clump, respectively and let r be the size of the dust particles forming the clump. Then

$$M_{cl} = \frac{4r\rho_0 L_{cl} H_{cl} \Delta\tau}{3 Q_{ext}}, \qquad (2)$$

where Q_{ext} is the extinction efficiency and ρ_0 is the density of individual dust particles. We will take $\Delta\tau = 0.4$, $Q_{ext} = 1$ (geometrical optics limit) and we will assume $\rho_0 = 1$ g cm^{-3} (solid ice density). We get limits on H from the modeling of the F ring, with a typical value of $H \sim 20$ km (Poulet et al. 2000), which is assumed to be the same for the clumps. Because of the Kepler shear, $W_{cl} \ll L_{cl}$ in general. Most of the observed clumps are unresolved, but some can extend over a few degrees, so we take a typical length of $L_{cl} \sim 2500$ km for the clumps, corresponding to a longitude interval of one degree. Since the main clumps detected in the Voyager images are uniformly distributed around the ring with typical lengths of 5000 to 13,000 km (Smith et al. 1982), the value of L_{cl} taken here (and thus, of $\dot{M}_{reg}$) probably corresponds to a lower limit.

Since these clumps are not persistent features, creation and destruction mechanisms are required over the observed time scales of at least 1 week and at most 3 months. Possible processes underlying such temporal evolution include drag forces and electromagnetic processes. Showalter et al. (1992), however, show that electromagnetic forces probably play an insignificant role in the dynamics of the F ring. Moreover, the Poynting–Robertson drag acting on micrometer-sized grains has significant effects only over thousands of years. Since the lifetime of the clumps is much shorter, the most obvious remaining mechanism is the Kepler shear.

A dynamically unconfined clump with azimuthal extent θ spreads at the rate $\dot{\theta} = 3n\Delta a/2a$, where Δa is assumed to be identical to the width of the clump W_{cl}, n is the mean motion, and a is the semimajor axis of the ring. This spreading causes the disappearance of the clump (by blending into the background average F ring) over a time scale of

$$T \sim \frac{\theta}{\dot{\theta}} \frac{\Delta\tau}{\tau} = \frac{2}{3}\left(\frac{\Delta\tau}{\tau}\right)\left(\frac{a\theta}{nW_{cl}}\right) \sim 500\left(\frac{\theta}{1°}\right)\left(\frac{1 \text{ km}}{W_{cl}}\right)\text{days}. \qquad (3)$$

Since the observed clumps extend over a few degrees at most and the lifetime is a few months (see discussion in Section 3.4), Eq. (3) yields a width W_{cl} in the range of a few tens of kilometers. This value is actually compatible with the Voyager observations, which give a width of about 50 km for the main strand of the F ring (Showalter et al. 1992, Murray et al. 1997). In other words, the observed lifetime of the clumps is compatible with a disruption caused by keplerian shear. We will take $\Delta a = W_{cl} \sim 50$ km as typical values. We will need the value of W_{cl} later, when we constrain the number and radius of the parent bodies embedded in the F ring (Eq. (10)).

From the different observations (N96, Roddier et al. 1996b, this work), we estimate that the detections of August 1995 imply a total of $N_{cl} \sim 10$ different clumps at any time in the F ring. Thus, Eq. (1), together with the numerical values discussed above, yield a total injection rate of

$$\dot{M}_{reg} \sim 5 \times 10^4 \left(\frac{r}{1 \,\mu\text{m}}\right) \text{g s}^{-1}. \qquad (4)$$

The flux Φ of meteoroids impacting the ring plane has been estimated by Durisen *et al.* (1996); see their Eq. (1). We find $\Phi \sim 5 \times 10^{-17}$ g cm^{-2} s^{-1} for the F-ring core (for $\tau \sim 0.1$). The impact yield Y (the ratio of the total ejecta mass to the projectile mass) is estimated from experiments with hypervelocity cratering on water ice targets. We use $Y = 10^4$ as a typical value. Based on the cross-sectional area of the core of the F ring $A_F = 10^{15}$–10^{16} cm^2 (width ~ 1 km, radius 140,200 km), we derive a mass erosion rate of

$$\dot{M}_{er} \sim A_F \Phi Y \sim 10^3 \text{ g s}^{-1}. \qquad (5)$$

Although the uncertainties on the quoted numbers may be large, the derived erosion rate still appears to be insufficient to explain the required mass injection rate of Eq. (4), unless $r \lesssim 0.05$ μm. Note also that the observed ejecta collected in meteoritic impact shots with icy particles yield typical particle sizes around $r \sim 10$ μm (Ip, 1995).

A recent estimate of Φ by Cuzzi and Estrada (1998) gives a bombarding flux about 10 times bigger than the value of Durisen *et al.* (1996) used here. Also, including the impacts onto the whole F ring increases the erosion rate. So, purely from the mass injection standpoint, the discrepancy between Eqs. (6) and (7) may be not so large. However, this micrometeoroid ejecta is in numerous small grains that would produce a continuous dust population rather than the discrete clumps seen, which would require larger projectiles and thus occur at a smaller rate (Showalter 1998). Thus a purely meteoritic origin for the largest clumps seems unlikely. This is why we turn to the hypothesis of clumps produced by collisions between parent bodies, embedded in the F ring, and covered by regolith.

4.2. Population of Parent Bodies: Number and Size

4.2.1. Model description. Our problem now is to explain the injection rate of Eq. (4) by collisions between parent bodies. In this case, the grains of the observed clouds result from a balance between collisional excavation and sweep-up by parent bodies. If N_p is the total number of parent bodies and $\dot{M}_{accr}$ is the mass accretion rate on a given parent body, this balance reads

$$N_p \dot{M}_{accr} = \dot{M}_{reg}. \qquad (6)$$

One unknown of the problem is N_p, and the other one is R_p, the radius of the parent bodies (on which the accretion rate $\dot{M}_{accr}$ eventually depends). Thus we need another equation to solve for both N_p and R_p.

This second constraint is provided by the number of collisions per unit time between any two parent bodies, N_{col}. As we saw before, there are about 10 clumps at a given time in the F ring, each with a lifetime of about $T = 2$ months. This requires on the average $N_{col} \sim 1/6$ collisions per day involving any one of the large particles of the F ring. The quantity N_{col} depends on both

N_p and R_p, which provides the second constraint we are looking for. This relation reads[2]

$$N_{col} \sim N_p n \tau_p \sim N_p^2 R_p^2 n / 2a\Delta a, \qquad (7)$$

where Δa is the width of the ring where the parent bodies are confined and τ_p the optical depth of the population of parent bodies. Formally, we should take into account the gravitational enhancement of the collision cross-section by $[1 + (\frac{V_{esc}}{V_{rel}})^2]$. However, we will see later that the relative velocity V_{rel} in the F ring and the escape velocity V_{esc} for the parent bodies are such that the focusing factor is certainly lower than 2. Moreover, we assume that the optically thin population of parent bodies is spatially distributed over three dimensions, which eliminates the two-dimensional case for which the motions of the particles would occur primarily in a plane.

If we assume that the particles' mutual gravitational attraction is the cause of accretion, the reaccretion rate can fall into two regimes: Regime 1, in which the random motion is the dominant mechanism for bringing material within the sphere of influence of the parent bodies, or Regime 2, where the dominant mechanism is the Kepler shear, i.e., where the random velocity is small.

The transition between the two regimes is analyzed by Greenberg *et al.* (1991), who define a minimal random velocity to get into Regime 1. In our case, we find that the random velocity must be larger than several tens of centimeters per second to get into Regime 1.

The relative velocity $V_{rel} = \sqrt{2}V_{ran} \sim an(e^2 + i^2)^{1/2}$ can reach several tens of meters per second if we take into account the eccentricity e and inclination i of the F ring, assuming noncorrelated (i.e., nonnested) orbits. By contrast, a conjunction with Prometheus induces relative velocities of only ~ 1 m s^{-1} across the F ring. Similarly, the thickness of the F ring (~ 20 km) yields an out-of-plane velocity of several tens of centimeters per second. Gravitational stirring by large bodies inside the F ring predicts relative velocities of the order of the escape velocities at the surface of these large bodies. Because the latter cannot have radii much larger than a few kilometers (see below) and assuming that they have densities comparable to or less than that of the ice, this yields relative velocities smaller than a few meters per second. On the other hand, the confinement of the F-ring core would indicate much lower random velocities. Since we have conflicting information on V_{rel}, we have considered here a range of speeds (see Table III and Fig. 5).

In Regime 1, the mass accretion rate on a parent body of radius R_p is given by

$$\dot{M}_{accr} = \pi S^2 V_{rel} \rho_{cl}, \qquad (8)$$

---

[2] Even in the low-velocity regime, studies by Wetherill and Cox (1985) show that the collision frequency changes by a factor of only 3.
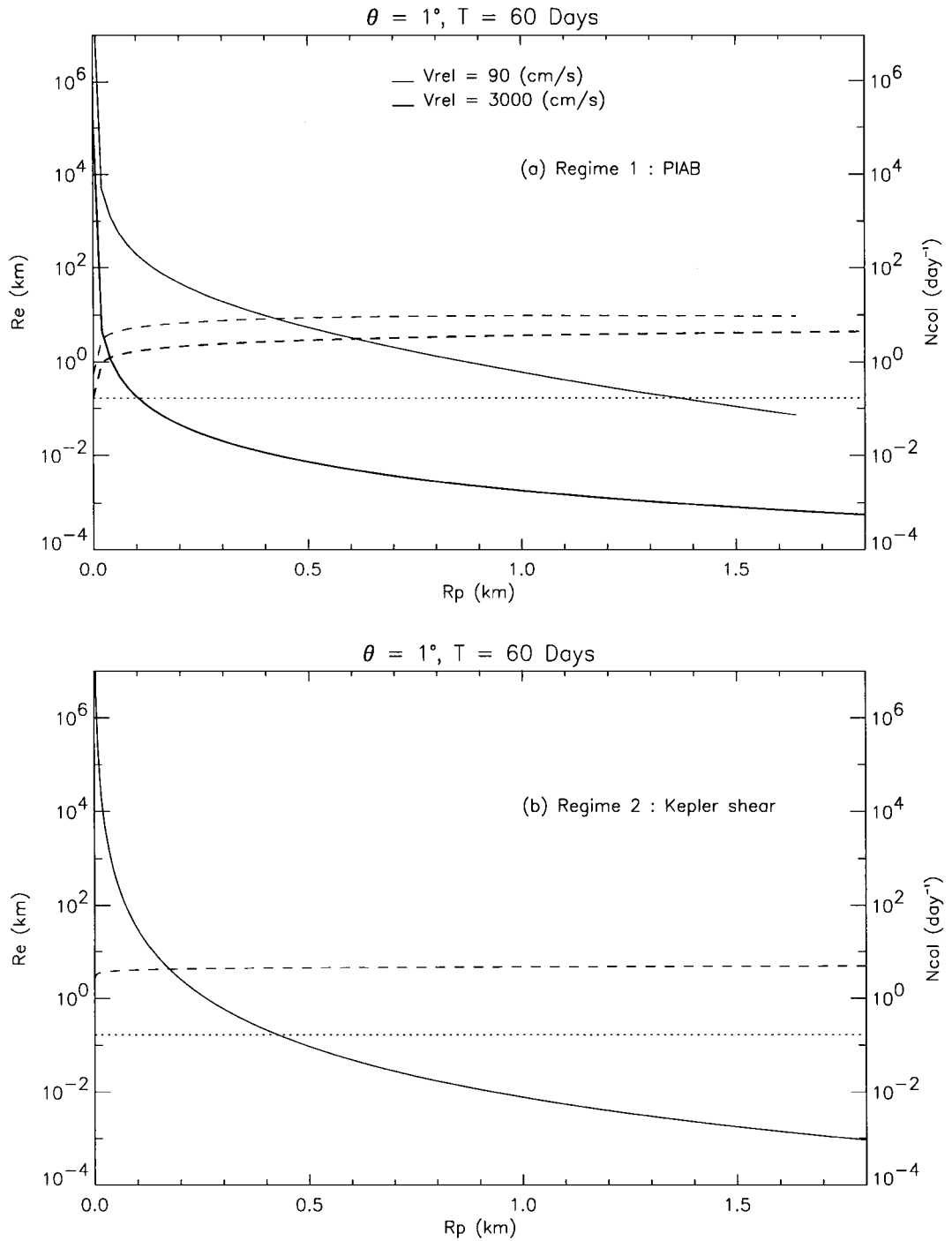
FIG. 5. (a) Number of collisions per day between any two parent bodies, N_{col} (solid lines), and the equivalent radius, R_e (dashed lines), vs the radius of the parent bodies, R_p, for two relative speeds. The horizontal dotted line defines $N_{col} = 0.16$ collisions day^{-1} estimated for the F ring. If V_{rel} is too small (here ≲90 cm/s), the determination of the accretion rate in the frame of Regime 1, for which the collision rate is computed under the assumption of "particle in a box" (PIAB) is invalid (b) Same as in (a), but in the case of Regime 2 (i.e., for lower V_{rel}).

where

$$\pi S^2 = \pi R_p^2 \left[1 + \left(\frac{V_{esc}}{V_{rel}} \right)^2 \right] \tag{9}$$

is the effective cross section of the parent body, and ρ_{cl} is the spatial density of the accretable material, i.e., the density of a typical clump, $\rho_{cl} = M_{cl}/L_{cl} W_{cl} H_{cl}$.

A condition must be fulfilled for a small particle touching the surface of a larger one to be attracted toward this surface against

TABLE III
Distribution of the Parent Bodies in Case of Regime 1 and Distributed over a Ring of Width 50 km

Parameter	$V_{rel} = 90$ cm/s	$V_{rel} = 3000$ cm/s
R_p (km)	$1.4^{+1.6}_{-0.4}$	$0.1^{+0.1}_{-0.05}$
N_p	300 ± 150	5000 ± 4000
R_e (km)	10^{+6}_{-2}	$1.7^{+3.3}_{-0.6}$
τ_p	$10^{-4} \pm 5 \times 10^{-5}$	$7 \times 10^{-6} \pm 5 \times 10^{-6}$
Meteoroid erosion time (years)	$\sim 10^8$	$\sim 10^7$

the tidal field of the planet (Longaretti 1989, Canup and Esposito 1995). For two F-ring particles of densities close to that of water ice, accretion is very likely to happen if the mass of the smaller particle is smaller than about 0.01 times the mass of the larger particle. This is the case for the regolith particles hitting the parent bodies considered here, so that reaccretion of the clouds of dust released during a collision should be very efficient. In our calculations, all the contacts between clump particles and parent bodies are assumed to result in reaccretion.

In Regime 2, we need the collision frequency appropriate to shear-dominated collisions. An expression for this low-velocity regime has been derived in the context of planetary accretion by Greenberg *et al.* (1991). More precisely, they derived the collision frequency by estimating the flow of small particles into the vicinity of the parent bodies due to keplerian shear as well as the gravitational cross section (the product of these two quantities giving the impact rate). Although it is valid only in a tide-free environment, we will use it here to estimate roughly the number and size of the parent bodies.

From Eqs. (1), (6), (8), and (9), and from the expression of ρ_{cl}, we derive for Regime 1:

$$N_p \pi R_p^2 \left[1 + \left(\frac{V_{esc}}{V_{rel}} \right)^2 \right] V_{rel} T = N_{cl} L_{cl} H_{cl} W_{cl}. \quad (10)$$

This equation simply states that the parent bodies have to sweep up, during the time T, the accumulated volume of the clumps, in order for a steady state to be reached. The numerical values of N_{cl}, L_{cl}, W_{cl}, H_{cl}, and T have been discussed before. Thus, Eq. (10) can be solved for a variety of V_{rel}, yielding N_p as a function of R_p. Equation (7) is then used to compute N_{col}. Finally, the equivalent radius R_e of a single body that would contain the mass of all of the parent bodies can be calculated as $R_e = N_p^{1/3} R_p$.

4.2.2. Results. The results obtained in the case of Regimes 1 and 2 are shown in Figs. 5a and 5b, respectively. The vertical axis at the right gives the value of N_{col}. The vertical axis at the left shows the equivalent radius R_e.

For a given height H_{cl}, and a given relative velocity V_{rel}, we can determine the radius R_p of the parent bodies necessary to produce one collision every 6 days. The results for Regime 1 are summarized in Table III.

The values of the parameters used above to derive N_p and R_p correspond to mean values, but they are subject to some degree of uncertainty. Thus, we examine our scenario further by considering two extreme cases, for which the input parameters are equal to their maximal or minimal values. First, we consider $T = 80$ days, $L_{cl} = 2500$ km, $W_{cl} = 45$ km, and $H_{cl} = 15$ km, and, second, $T = 50$ days, $L_{cl} = 7500$ km, $W_{cl} = 55$ km, and $H_{cl} = 25$ km. The errors bars in Table III are defined by these two extreme models.

Overall, considering the width of the main component of the F ring to be $\Delta a \sim 50$ km (Murray *et al.* 1997), our model shows that the radius of the parent bodies strongly depends on the relative velocity, V_{rel}, and must range from 100 m for high relative velocities to a few kilometers for the lowest relative velocities. In any case, R_p is never larger than 3 km in our model (Table III). This is compatible with the upper limit provided by the Voyager images (about 10 km; see Synnott 1986).

In the case of Regime 2, Fig. 5b shows that the value of R_p also remains within the above limits (i.e., a few hundred meters).

4.3. Thickness of the Regolith

We can derive another property of the parent bodies, namely the thickness z, of the regolith covering the parent bodies. We assume that collisions between two parent bodies release previously accumulated debris, without significant erosion or creation of additional debris. The mass of regolith of density ρ_{reg} lost during a collision is then similar to the mass of the clump, which gives a relation between z, the radius of the parent bodies, and the typical size, r, of a regolith particle:

$$4\pi R_p^2 \rho_{reg} f z = M_{cl}/2. \quad (11)$$

Here, f is the fraction of regolith released when two parent bodies collide. Note that each parent body contributes to half the mass of the clump M_{cl}. From Eq. (2), we can derive

$$z = \frac{1}{6\pi} \left(\frac{\rho_0}{\rho_{reg}} \right) \left(\frac{L_{cl} H_{cl} \Delta \tau}{Q_{ext} R_p^2} \right) \left(\frac{r}{f} \right). \quad (12)$$

We recall that a typical value of $\Delta \tau \sim 0.4$ is obtained from the observations. As discussed in Section 4.1, we adopt $H_{cl} = 20$ km and $L_{cl} = 2500$ km. We assume a regolith density ρ_{reg} of 0.1 g cm^{-3}, corresponding to the density of snow (Weidenschilling *et al.* 1984). The determination of f is difficult, since there are few experimental data for ejecta production. We retain the estimate of Canup and Esposito (1995), who give $f = 0.12$ when two like-sized objects collide. Note, however, that the two factors $f z$ always appear together in this calculation, so that it is easy to derive alternative values of z from other values of f. However, we prefer to keep explicitly the factor $f = 0.12$ for the following reason. Even though a small fraction of regolith may be released during a given collision, it may be that various layers of regolith participate in different collisions, so that the total reservoir of
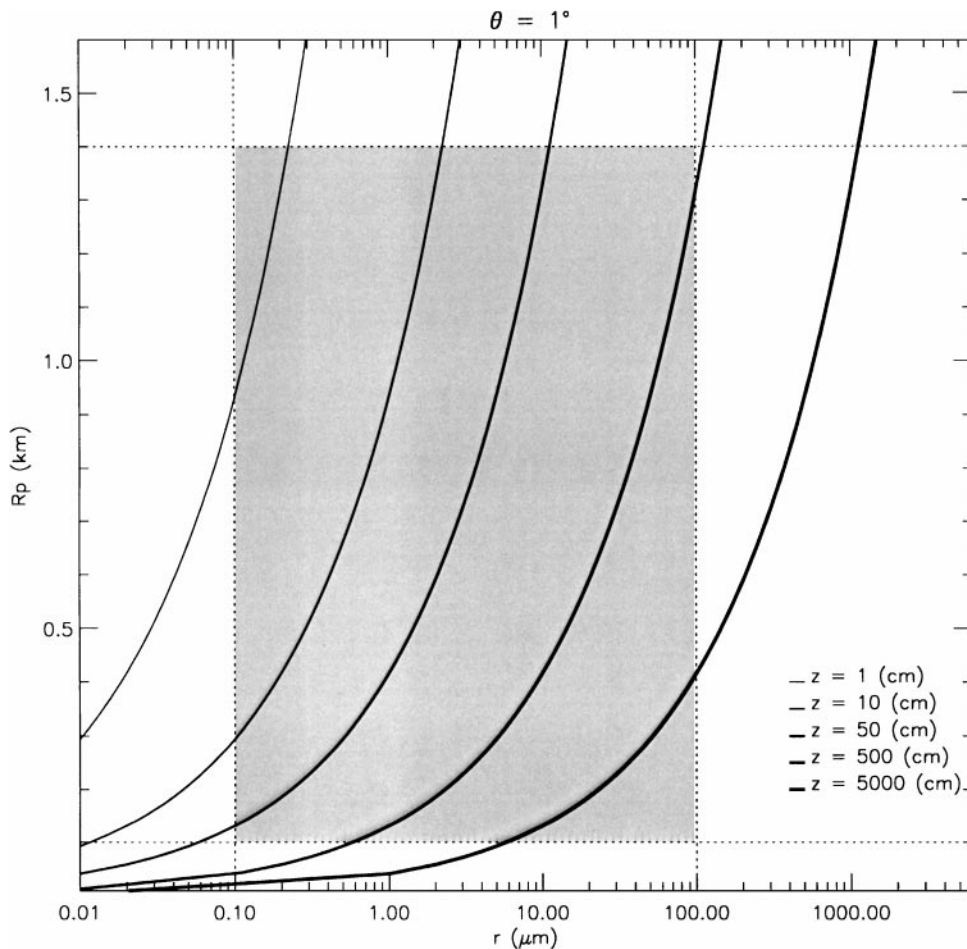
FIG. 6. The relation between the radius, R_p, of the parent bodies and the radius, r, of the regolith particles is plotted for several regolith thicknesses ($1 \leq z \leq 5000$ cm). These relations are obtained for a clump of length $1°$. The shaded zone defines the intersection of the possible parent radii with the likely sizes of the regolith particles. See the text for a description of the model.

regolith may be larger than the small fraction of dust released during one collision.

The results presented in Fig. 6 illustrate which combinations of r, R_p, and z are able to satisfy Eq. (12). We now relax the condition on the particle size, r, which was taken to be equal to $r = 10~\mu$m in the case of meteoritic excavation. By contrast, regolith particles may have radii distributed over a much wider range due to long-term collisional and accretional processes. This range ($0.1 < r < 100~\mu$m) is marked in Fig. 6 by the two vertical dashed lines. The previous section gives constraints on the size of the parent bodies ($0.1 < R_p < 1.4$ km), which defines the shaded zone in Fig. 6. The curves then show the relationship between R_p and r (Eq. (12)) for various values of z.

Thus, the mass of the clumps can be supplied by collisions between parent bodies if the layers of regolith have a thickness ranging from a few tens of centimeters to a few meters. This is a reasonable range, considering that the parent bodies have much larger radii of $\sim$100 m to 1.5 km. For comparison, the average regolith depth on a ringmoon (with a typical radius $\sim$100 m) in

Neptune's Adams ring is estimated to be about 8 m by Canup and Esposito (1995), using the same fraction $f = 0.12$ as adopted here.

5. CONCLUSIONS

We have observed four saturnian objects (S/1995 S5, 1995 S6, 1995 S20, and Arc10) near the orbit of the F ring. Indeed, the number of planetocentric measurements for S5 (23 so far) now yield an orbital radius which is consistent, within the error bars, with that of the F ring. The object Arc10 is also obviously linked to the F ring (Fig. 2). This is not yet proved for S6 and S20, considering the present uncertainties in the orbital elements. These observations, when linked to other data sets, may better constrain the dynamics of the F ring.

In the meantime, only S3 and S6 can be matched between May and August 1995 with a unique F ring object (N96) if one assumes that these objects have the F-ring mean motion. Similarly several bright clumps were seen within the Fring during the

Voyager visits in 1980 and 1981, and none of them can be clearly linked over the 9-month period separating the two encounters. Finally, the objects detected in 1995 are all bright enough not to have been overlooked by the Voyager spacecraft, if they were a swarm of permanent satellites. Altogether, this indicates that the F-ring objects are transient in nature, with lifetimes of at most a few months.

In this paper, we have envisioned a situation in which parent bodies embedded in the F ring sporadically release clouds of loosely bound regolith material when they collide with each other, while sweeping up debris between successive collisions. We show that the RPX and Voyager observations of transient objects can be explained if there are several thousands of 100 -m-sized (or several hundreds of $\sim$1-km-sized) parent bodies in the F ring. The thickness of the regolith on the surface of these bodies ranges between a few tens of centimeters to a few meters. Moreover, it appears that the Keplerian shear can spread the clumps longitudinally over a time scale less than a few months, which is compatible with the Voyager and present observations. Finally, gravitational scatterings by bodies of a few kilometers in radius could maintain a velocity dispersion consistent with the $\sim$20 km thickness of the F ring (Poulet *et al.* 2000).

Several authors (Lissauer and Peale 1986, Cuzzi and Burns 1988, Showalter *et al.* 1992, Hänninen 1993, Murray *et al.* 1997) have postulated the existence of small satellites or large particles ($R_p < 10$ km) within the F ring in order to explain various aspects of its strange morphology. Similar conclusions hold for Saturn's G ring (Canup and Esposito 1997) and Neptune's rings (Canup and Esposito 1995).

These large particles would contain most of the mass of the F ring and will erode under micrometeoroid bombardment. We can compute the mass flux of the meteoroids using Eq. (1) of Durisen *et al.* (1996) for the parent bodies. The gross erosion rate, i.e., with no reaccretion of the ejecta, indicates that the population of parent bodies with radius $\sim$100 m (or a few kilometers) could maintain the F ring for at least a few millions (or a few hundreds of millions) of years (see Table III). In reality, this lifetime is rather academic and probably an underestimate, as reaccretion will bring most of the ejected dust back on to the particles, as discussed in this paper.

The very existence of a population of large-sized bodies in the F ring remains to be explained. A possibility is that they represent cohesive fragments from previous catastrophic disruption events. Note that because of the criterion of accretion proposed by Canup and Esposito (1995)—see Section 4.2—the large parent bodies do not accrete easily when they collide with each other. This could explain why they do not rapidly reform a single satellite.

They are several limitations to our model. First, only one parent body size is considered. A wide distribution of sizes could lead to aggregates of loosely bound large particles, providing more complex scenarios. Also, we have ignored collisions between regolith particles, which could lead to sticking. There is some experimental evidence, however, that sticking between dusty aggregates, even at low velocities, is not very efficient (Blum and Münch 1993). Note finally that the gravitational influences of Prometheus and Pandora have not been considered here. In particular the possible confinement of the F ring core by the two satellites, the presence of numerous resonances, the possibility of chaotic motion, and their effects on the collision rate between the parent bodies have yet to be studied.

Our model accounts in a natural way for the steady state interaction between the parent bodies and the production of clumps on a short time scale (several months). It does not address the question of the stability of the F ring over periods of hundreds of years, over which the ring could be "transient" (see Cuzzi and Burns 1988). Nevertheless, monitoring and understanding the short-term dynamical evolution of the F ring is essential for casting light on the long-term history of narrow and dusty rings and perhaps also on the planetary accretion process.

REFERENCES

Biretta, J. A., C. Burrows, J. Holtzman, I. Heyer, M. Stevens, S. Baggett, S. Casertano, M. Clampin, A. Fruchter, H. Ferguson, R. Gilliland, R. Griffiths, J. Krist, K. Noll, C. O'Dea, M. Stiavelli, A. Suchkov, J. Surdej, and B. Withmore 1996. *WFPC2 Instrument Handbook*, Version 4.0. Space Telescope Science Inst., Baltimore, MD.

Blum, J., and M. Münch 1993. Experimental investigations on aggregate–aggregate collisions in the early solar nebula. *Icarus* **106**, 151–167.

Bosh, A. S., and C. B. Olkin 1997. Search for inclined features in Saturn's rings. *Bull. Am. Astron. Soc.* **29**, 1000.

Bosh, A. S., and A. S. Rivkin 1996. Observations of Saturn's inner satellites during the May 1995 ring-plane crossing. *Science* **272**, 518–521.

Campbell, J. K., and J. D. Anderson 1989. Gravity field of the saturnian system from *Pioneer* and *Voyager* tracking data. *Astron. J.* **97**, 1485–1495.

Canup, R. M., and L. W. Esposito 1995. Accretion in the Roche zone: Coexistence of rings and ringmoons. *Icarus* **113**, 331–352.

Canup, R. M., and L. W. Esposito 1997. Evolution of the G ring and the population of macroscopic ring particles. *Icarus* **126**, 28–41.

Cuzzi, J. N., and J. A. Burns 1988. Charged particle depletion surrounding Saturn's F ring: Evidence for a moonlet belt? *Icarus* **74**, 284–324.

Cuzzi, J. N., and P. A. Estrada 1998. Compositional evolution of Saturn's rings due to meteoroid bombardment. *Icarus* **132**, 1–35.

Durisen, R. H., P. W. Bode, S. G. Dyck, J. N. Cuzzi, J. D. Dull, and J. C. White II 1996. Ballistic transport in planetary ring systems due to particle erosion mechanisms. *Icarus* **124**, 220–236.

Greenberg, R., W. F. Bottke, G. B. Valsecchi, and A. Carusi 1991. Planetary accretion rates: Analytical derivation. *Icarus* **94**, 98–111.

Hänninen, J. 1993. Numerical simulations of moon–ringlet interaction. *Icarus* **103**, 104–123.

Holtzman, J. A., J. Hester, S. Casertano, J. T. Trauger, A. M. Watson, G. E. Ballester, C. J. Burrows, J. T. Clarke, D. Crisp, R. W. Evans, J. S. Gallagher III, R. E. Griffiths, J. G. Hoessel, L. D. Matthews, J. R. Mould, P. A. Scowen,

K. R. Stapelfeldt, and J. A. Westphal 1995. The performance and calibration of WFPC2 on the Hubble Space Telescope. *Pub. Astron. Soc. Pacific* **107**, 156–178.

Ip, W.-H. 1995. Implications of meteoroid-ring interactions for observations of the 1995 Saturn ring plane crossing. *Icarus* **117**, 212–215.

Lissauer, J. J., and S. J. Peale 1986. The production of "braids" in Saturn's F ring. *Icarus* **67**, 51–73.

Longaretti, P-Y. 1989. Saturn's main ring particle size distribution: An analytic approach. *Icarus* **81**, 51–73.

McGhee, C. A., P. D. Nicholson, R. G. French, and K. J. Hall 1998. HST observations of Saturn's F ring region during the 1995 ring-plane crossings. *Bull. Am. Astron. Soc.* **30**, 1040.

Murray, C. D., M. K. Gordon, and S. M. G. Winter 1997. Unraveling the strands of Saturn's F ring. *Icarus* **129**, 304–316.

Nicholson, P. D., C. A. McGhee, M. R. Showalter, L. Dones, R. G. French, S. M. Larson, J. J. Lissauer, P. Seitzer, B. Sicardy, and G. E. Danielson 1995. Satellites of Saturn. *IAU Circ. 6243*.

Nicholson, P. D., M. R. Showalter, L. Dones, R. G. French, S. M. Larson, J. J. Lissauer, C. A. McGhee, P. Seitzer, B. Sicardy, and G. E. Danielson 1996. Observations of Saturn's ring-plane crossings in August and November 1995. *Science* **272**, 509–515.

Poulet, F., B. Sicardy, J. L. Beuzit, and P. Prado 1997. Observations of Saturn's inner satellites during the August 1995 ring-plane crossing. In *Dynamics and Astrometry of Natural and Artificial Celestial Bodies*, IAU Colloquium 165, pp. 525–530. Kluwer Academic, Dordrecht.

Poulet, F., B. Sicardy, C. Dumas, L. Jorda, and D. Tiphène 2000. The crossings of Saturn ring plane by the Earth in 1995: Ring thickness. *Icarus*, in press.

Roddier, F., A. Brahic, C. Dumas, C. Ferrari, J. E. Graves, M. J. Norhcott, T. Owen, L. Perret, C. Roddier, and P. Thebault 1996a. Satellites of Saturn. *IAU Circ. 6407*.

Roddier, C., F. Roddier, A. Brahic, J. E. Graves, M. J. Norhcott, and T. Owen. 1996b. Satellites of Saturn. *IAU Circ. 6515.*

Salo, H. 1992. Gravitational wakes in Saturn's rings. *Nature* **359**, 619–621.

Showalter M. R. 1995. "*Saturn Viewer*" software at the Planetary Data System's *Ring Node*. Located at http://ringside.arc.nasa.gov.

Showalter, M. R. 1997. Dynamics of clumps in Saturn's F ring. *Bull. Am. Astron. Soc.* **29**, 999.

Showalter, M. R. 1998. Detection of centimeter-sized meteoroid impact events in Saturn's ring. *Science* **282**, 1099–1102.

Showalter, M. R., and J. A. Burns 1982. A numerical study of Saturn's F-ring. *Icarus* **52**, 526–544.

Showalter, M. R., J. B. Pollack, M. E. Ockert, L. R. Doyle, and J. B. Dalton 1992. A photometric study of Saturn's F ring. *Icarus* **100**, 394–411.

Sicardy, B., J.-L. Beuzit, F. Poulet, and P. Prado 1995. Detection of 1995S6. *IAU Circ. 6269.*

Sicardy, B., P. D. Nicholson, G. E. Danielson, L. Dones, R. G. French, S. M. Larson, J. J. Lissauer, C. A. McGhee, P. Seitzer, and M. R. Showalter 1996b. Hubble Space Telescope observations of Saturn during the August and November 1995 ring plane crossings. In *Science with the Hubble Space Telescope II* (P. Benvenuti, F. D. Machetto, and E. J. Schreier, Eds.), pp. 546–552. Space Telescope Science Institute, Baltimore.

Sicardy, B., F. Poulet, J. L. Beuzit, and P. Prado 1996a. Detection of 1995S5. *IAU Circ. 6395.*

Smith, B. A., L. Soderblom, R. Batson, P. Bridges, J. Inge, H. Masursky, E. Shoemaker, R. Beebe, J. Boyce, G. Briggs, A. Bunker, S. Collins, C. Hansen, T. Johnson, J. Mitchell, J. Terrile, A. Cook, J. Cuzzi, J. Pollack, G. E. Danielson, A. Ingersoll, M. Davies, G. Hunt, D. Morrison, T. Owen, C. Sagan, J. Veverka, R. Strom, and V. Suomi 1982. A new look at the Saturn system: The Voyager 2 images. *Science* **215**, 504–537.

Synnott, S. P. 1986. Evidence for the existence of additional small satellites of Saturn. *Icarus* **67**, 189–204.

Weidenschilling, S. J., C. R. Chapman, D. R. Davis, and R. Greenberg 1984. Ring particles: Collisional interactions and physical nature. In *Planetary Rings* (R. Greenberg and A. Brahic, Eds.), pp. 367–416. Univ. of Arizona Press, Tucson.

Wetherill, G. W., and L. P. Cox S. P. 1985. The range of validity of the two-body approximation in models of terrestrial planet accumulation. *Icarus* **63**, 290–303.